A simple mathematical model of rhegmatogenous retinal detachment

Damiano Natali [a], Rodolfo Repetto [a], Jennifer H. Tweedy [b],
Tom H. Williamson [c,d], Jan O. Pralits [a,*]

[a] Università degli Studi di Genova, DICCA, via Montallegro 1, 16145 Genova, Italy
[b] Imperial College London, Department of Bioengineering, London SW7 2AZ, UK
[c] Retina Surgery, 50-52 New Cavendish Street, London W1G 8TL, UK
[d] NHS, St Thomas Hospital, London SE1 7EH, UK

ARTICLE INFO

ABSTRACT

The conditions under which rhegmatogenous retinal detachment occurs are poorly understood, which hampers the success rates of surgery. Fluid dynamical effects play a major role, and in this paper we analyse the tendency for the retina to detach further in both the case of a free flap giant retinal tear (GRT) and in the case of a retinal hole (RH). For this purpose we use a mathematical model to investigate the interaction between the fluid flow and the detached retina during saccadic eye movements. The governing equations are solved numerically using a code developed ad hoc. An idealised two-dimensional geometry is used and realistic values of almost all governing parameters are taken from the literature. For the cases of both GRT and a RH we investigate the tendency for the detachment to progress, analysing two different saccadic motions, different lengths of the detached retina, different attachment angles and, in the case of a RH, different hole diameters. In both cases we find that increasing the length of the detached retina increases the tendency for further detachment, while in the RH case, changing its diameter has little or no effect. We also find the existence of an attachment angle that maximises the tendency to detach, and the model indicates that RHs are more prone to detach further than GRTs. In spite of the fact that the model is highly idealised the results agree qualitatively well with the available clinical evidence.

© 2018 Elsevier Ltd. All rights reserved.

1. Introduction

Rhegmatogenous retinal detachment (RRD) occurs in approximately 10: 100 000 of the population (Mitry et al., 2009). It is caused by the appearance of a retinal break or breaks in the peripheral retina, which are associated with the accumulation of subretinal fluid, causing detachment of the neurosensory retina. Traction on the retina from separation of the posterior vitreous is thought to create the retinal break. However, traction alone cannot explain the development of the retinal break into full RRD. For this reason it has been postulated that saccadic eye movements create currents in the liquefied vitreous, which cause the retina to lift away. This process is poorly understood and has not been extensively investigated from the mechanical point of view. Unchecked retinal detachment results in blindness. Although surgical interventions lead to successful reattachment in many cases, there is often uncertainty surrounding the mechanism of action of these surgical methods, resulting in suboptimal success rates. It should be noted that both the typical clinical presentation and the rate of

* Corresponding author.
  E-mail address: jan.pralits@unige.it (J.O. Pralits).

Table 1
Parameter values used for the simulations and corresponding references when available.

Quantity	Value	Reference
Properties of the retinal flap		
Density ρ_S^*	1300 kg/m^3	
Length L^*	1.5–2.5 mm	
Thickness h^*	70 μm	Alamouti and Funk, 2003; Foster et al., 2010; Ethier et al., 2004; Bowd et al., 2000; Wollensak and Eberhard, 2004; Dogramaci and Williamson, 2013
Young's modulus E^*	$1.21 \cdot 10^3$ N/m^2	Jones et al., 1992; Wollensak and Eberhard, 2004; Reichenbach et al., 1991; Sigal et al., 2005
Bending stiffness $K_b^* = E^* h^{*3}/12$	$3.46 \cdot 10^{-11}$ Nm^2	
Properties of the fluid		
Density ρ_F^*	1000 kg/m^3	Foster et al., 2010
Dynamic viscosity μ^*	$1.065 \cdot 10^{-3}$ kg/ms	Foster et al., 2010

progress of a retinal detachment vary amongst different subjects. The risk of total retinal detachment is important as this affects the anatomical and visual outcome (Williamson et al., 2013, 2014).

In the present study, we model the effects of fluid flow due to saccadic eye motion on a two-dimensional construct of retinal detachment. Various parameters are examined to determine their effects on the elevation of the retina and improve our understanding of what causes or increases the tendency of the retina to detach. As in similar works (Peskin, 2002; Zhu and Peskin, 2002; Kim and Peskin, 2007; Natali et al., 2016), an immersed boundary (IB) method has been used to model elastic bodies interacting with a viscous incompressible fluid. Such a method has been used in various applications, such as cardiac valves (Kovacs et al., 2001) and animal locomotion (Fauci and Peskin, 1988), but this is the first time, to the authors knowledge, it has been used in the context of retinal detachment modelling. Previous works regarding the retina include calculating the shear stress on the retinal surface (Angunawela et al., 2011; Eames et al., 2010; Repetto et al., 2010a; Meskauskas et al., 2012; Abouali et al., 2012; Modarreszadeh and Abouali, 2014), gas diffusion in the vitreous cavity (Shunmugam et al., 2011), silicone oil usage (Dogramaci and Williamson, 2013; Isakova et al., 2014), retinal tractions (Repetto et al., 2010b) and peeling of membranes from the retinal surface (Dogramaci and Williamson, 2013; Bottega et al., 2013), just to mention a few. In order to study the tendency of the retina to further detach from the underlying choroid, due to the combined actions of the forces and moment at the attachment point(s) arising from the interaction between the detached retina and the surrounding fluid, we borrow a simple model from geotechnics of a structure on an elastic foundation (Winkler, 1867). The model assumes that the foundation can be described as a system of identical, mutually independent, closely spaced, discrete and linearly elastic springs. The model allows us to evaluate the displacement of the foundation, which is then analysed as a function of the parameters of interest. We believe that this study, first of its kind in that a fully coupled fluid–structure interaction model has been applied, despite the various approximations it is based on, gives insight on how the tendency of RRD progress depends on parameters, such as amplitude of the saccade, length of the detached retina, detachment angle, and hole diameter (in the case of a RH).

The paper is organised as follows. Section 2 describes the geometry and mechanical properties of the retina and the surrounding fluid as well as the saccadic eye motion. In Section 3 the governing equations for the fluid and the structure are presented along with the elastic foundation model. The numerical results are presented in Section 4 and conclusions are drawn in Section 5.

2. Geometry and mechanical properties

In this work we use simplified geometrical models to study the dynamics of detached retinal flaps induced by rotations of the eye. Specifically, we consider the two different cases depicted in Fig. 1a,b, and we use mathematical models of these simplified geometries to determine the effect of fluid flow on detachment progression. In particular, we use a two-dimensional approximation of the geometry and of the fluid flow, neglecting three-dimensional effects. Within our two-dimensional context the retinal flap is described as a slender, massive, inextensible, one-dimensional structure, with a fixed bending stiffness. In reality a retinal flap with length $L^* = 2$ mm, which is the baseline value used in this work, has an aspect ratio (thickness to length ratio) of approximately 1/30, justifying the slender-body assumption. Geometrical and mechanical properties of the retinal flap are presented in Table 1. The bending stiffness of the retina K_b^* is obtained from the value of the Young's modulus E^*, which has been computed by several authors (Jones et al., 1992; Wollensak and Eberhard, 2004; Reichenbach et al., 1991; Sigal et al., 2005) and the thickness h^*, on the basis of the relationship: $K_b^* = E^* h^{*3}/12$. Note that here superscript $*$ denotes dimensional variables and parameters. The inextensibility of the retina is an approximation and justified by the fact that no data regarding stretching of the detached retina can be found in the literature.

We model the retinal surface as a flat rigid wall, and neglect curvature effects. Moreover, we assume that the region occupied by the liquefied vitreous extends to infinity in the direction orthogonal to the retinal plane. The above assumptions are acceptable if the length of the flap is much smaller than the radii of curvature of the wall. In the present case the radius r^* of the vitreous chamber is approximately 12 mm, and the corresponding ratio L^*/r^* is between 0.125 and 0.21,
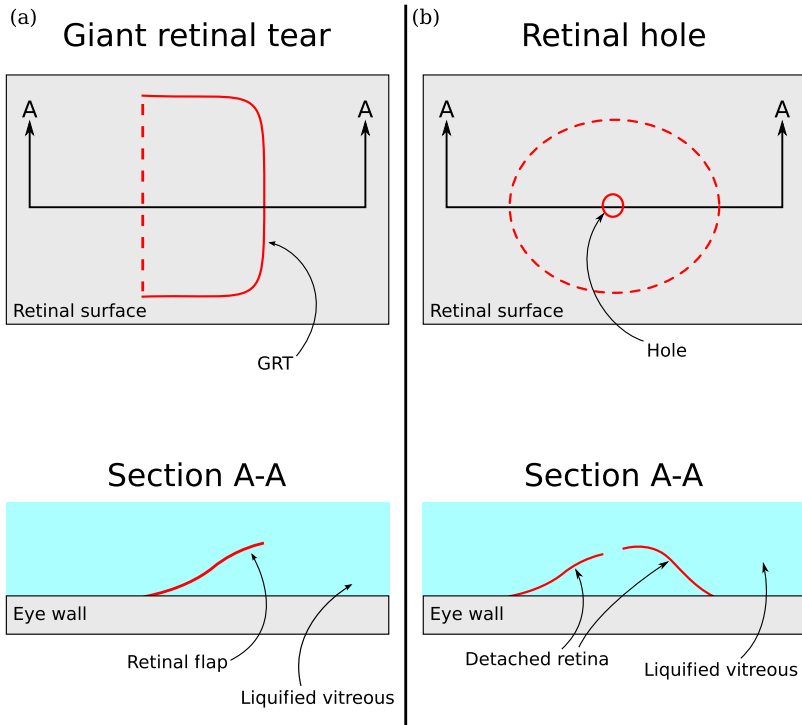
Fig. 1. Sketches of the domains considered: (a) free-flap giant retinal tear (GRT) which by definition has an aspect ratio length/circumferential extent $\ll 1$ (the figure is not in scale), (b) retinal hole (RH). The top panel shows a plan view where the dashed line denotes the attachment line, and the bottom shows a cross-section through the retina in each case, which is used for the numerical model.

based on the values of L^* used in this work. However, inclusion of wall curvature and finite size of the domain would complicate considerably the numerical calculations and this is left aside in the context of this first exploratory work. A similar assumption was done in previous models of retinal detachment (Foster et al., 2010; Foster, 2011)

The liquefied vitreous is modelled as a purely viscous fluid with the same mechanical properties as water and we assume that fluid flow is generated by motion of the retinal surface (wall) along its plane. Specifically, we consider a single saccadic eye rotation. The angular velocity of the eye globe is modelled employing the polynomial law proposed by Repetto et al. (2005) which was also used by Abouali et al. (2012). The wall linear velocity from this angular velocity is obtained by multiplying it by the radius of the vitreous chamber. We use saccadic rotations of 8 and 15 degrees, which have a duration of 0.045 s and 0.062 s, respectively. The corresponding maximum linear wall velocities are 0.061 m/s and 0.082 m/s, respectively. An example of such a motion is presented in Fig. 2.

The first case we consider is a free flap giant retinal tear (GRT), consisting of a single detached flap with 90 degrees or more of circumferential extent, see Fig. 1a. Note that a realistic aspect ratio (flap length to circumferential extent) is at least 1/40, which makes the two-dimensional model a reasonable approximation. The sketch in Fig. 1a has a much smaller aspect ratio for practical reasons.

We also consider a retinal hole, in which case the cross-section consists of two retinal flaps, see Fig. 1b. In order to mimic the three-dimensionality of the hole configuration we assume that the tips of the two flaps are connected to each other by a virtual linear elastic spring that exerts a force when stretched but not when compressed. Its effect is thus to limit the distance between the tips of the two flaps to that of the initial diameter, but they are free to get closer to each other. The idea is to allow for deformations of the retinal surface and account for buckling of the detached retinal surface. For simplicity, we assume that a generic buckling, causing a deformation in the third dimension, will make the two tips come closer to each other. The value of the spring constant was chosen such that the relative difference between the maximum distance between the filament tips, and the initial diameter, did not exceed 10^{-2}. This was obtained by setting the value of the spring constant equal to that of K_b^*.

The initial configuration of each case (GRT and RH) are straight filaments clamped at a certain angle θ, see Fig. 3. This is obviously an approximation since the real case would be a filament with continuous curvature, possibly tangent to the underlying choroid. In this first exploratory work this helps, however, to clearly parametrise the tendency of the retinal detachment on the initial detached state.

We finally assumed a flap density of ρ_S^* of 1300 kg/m³, which is probably slightly higher than the reality; however, owing to limitations of the mathematical method employed we cannot consider cases in which the density of the solid is too close
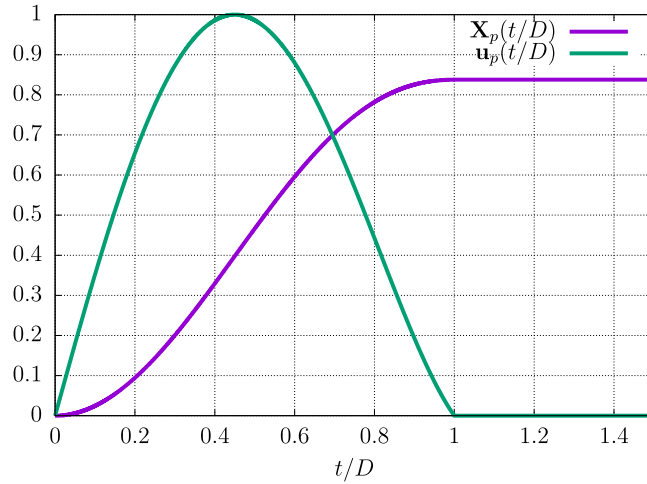
Fig. 2. Position $\mathbf{X}_p$ and normalised velocity $\mathbf{u}_p$ of the wall during a saccadic motion of duration D. In this investigation saccadic rotations of 8 and 15 degrees, which have a duration of 0.045 s and 0.062 s, respectively, are used. The corresponding maximum linear wall velocities are 0.061 m/s and 0.082 m/s, respectively.
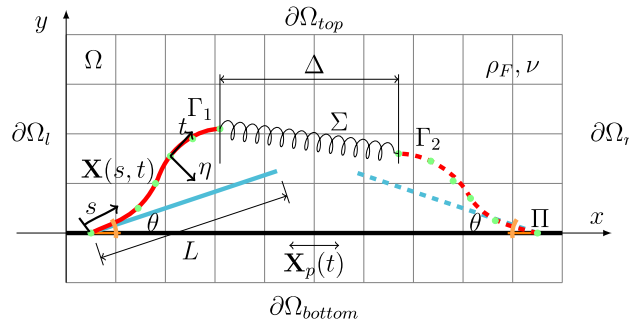

Fig. 3. Schematics of the numerical model. Flaps $\Gamma_{1,2}$ (in red, initial condition in cyan) are clamped at a fixed angle θ to an underlying plate Π that moves with a prescribed saccadic motion $\mathbf{X}_p(t)$. (For interpretation of the references to colour in this figure legend, the reader is referred to the web version of this article.)

to that of the fluid. Moreover, since little is known regarding the value of the density of the retina, and its variability, we do not consider our choice a large limitation. In the results section we show that the numerical results are quite insensitive to small variations of the value of ρ_S^*.

3. Governing equations

The governing equations for the fluid and the structure are similar to those found in Natali et al. (2016). We model the detached retina as a one-dimensional inextensible elastic filament of length L^*, with density ρ_S^* and bending rigidity K_b^*, exposed to a viscous incompressible fluid of density ρ_F^*, kinematic viscosity ν^* which is set into motion by a saccadic movement of the wall with maximum velocity U^*. The governing equations for the fluid, here given on dimensionless form, are

$$\frac{\partial \mathbf{u}}{\partial t} + (\mathbf{u} \cdot \nabla)\mathbf{u} = -\nabla p + \frac{1}{Re}\nabla^2 \mathbf{u} + \mathbf{f}, \tag{1}$$

$$\nabla \cdot \mathbf{u} = 0, \tag{2}$$

where $\mathbf{f}(\mathbf{x}, t)$ is an appropriate volume forcing to enforce the no-slip condition on the filament. The velocity field is denoted by $\mathbf{u}(\mathbf{x}, t)$, $p(\mathbf{x}, t)$ is the pressure field and $Re = U^* L^* \rho_F^* / \mu^*$ is the Reynolds number. Here $\mathbf{x} = (x, y) \in \Omega$ are the Cartesian coordinates, with x and y denoting the streamwise and wall-normal direction, respectively, see Fig. 3. The governing

equations for a filament are written in a Lagrangian form. The equations of motion are

$$\rho_1 \frac{\partial^2 \mathbf{X}}{\partial t^2} = \frac{\partial}{\partial s}\left(T\frac{\partial \mathbf{X}}{\partial s}\right) - \frac{\partial^2}{\partial s^2}\left(\gamma\frac{\partial^2 \mathbf{X}}{\partial s^2}\right) - \mathbf{F}, \tag{3}$$

where T is the tension force along the filament axis, $\gamma = K_b^*/(\rho_1^* U^{*2} L^{*2})$ is the dimensionless bending stiffness, $\rho_1^* = (\rho_S^* - \rho_F^*)h^*$ is the difference between the filament- and fluid densities, h^* is the filament thickness, and $\mathbf{F}$ is the Lagrangian forcing exerted on the filament by the surrounding fluid. Further, $s \in \Gamma$ denotes the Lagrangian curvilinear coordinate, where Γ is the body surface. The inextensibility condition (see Huang et al., 2007) is expressed by

$$\frac{\partial \mathbf{X}}{\partial s} \cdot \frac{\partial \mathbf{X}}{\partial s} = 1. \tag{4}$$

In the present study, as in other related investigations (e.g. Huang et al., 2007), the tension force T is determined by the constraint of the inextensibility condition. Using Eqs. (3) and (4), the equation for T is derived as

$$\frac{\partial \mathbf{X}}{\partial s} \cdot \frac{\partial^2}{\partial s^2}\left(T\frac{\partial \mathbf{X}}{\partial s}\right) =$$
$$\frac{1}{2}\frac{\partial^2}{\partial t^2}\left(\frac{\partial \mathbf{X}}{\partial s} \cdot \frac{\partial \mathbf{X}}{\partial s}\right) - \frac{\partial^2 \mathbf{X}}{\partial t \partial s} \cdot \frac{\partial^2 \mathbf{X}}{\partial t \partial s} - \frac{\partial \mathbf{X}}{\partial s} \cdot \frac{\partial}{\partial s}(\mathbf{F}_b - \mathbf{F}). \tag{5}$$

On the right hand side of Eq. (3) the first two terms represent the tensional $\mathbf{F}_s$ and bending terms $\mathbf{F}_b$. The last term represents the Lagrangian forces exerted by the fluid on the structure, obtained by means of Eqs. (6)–(8)

$$\mathbf{F} = (\mathbf{F}_{\alpha\beta} \cdot \mathbf{n})\mathbf{n} + (\mathbf{F}_{\alpha\beta} \cdot \boldsymbol{\tau})\boldsymbol{\tau}, \tag{6}$$

where $\mathbf{n}$ and τ are the local normal and tangential unit vectors,

$$\mathbf{F}_{\alpha\beta}(s,t) = \alpha\int_0^t\left(\mathbf{U_{ib}} - \frac{\partial \mathbf{X}}{\partial \mathbf{t}}\right)dt + \beta\left(\mathbf{U_{ib}} - \frac{\partial \mathbf{X}}{\partial \mathbf{t}}\right), \tag{7}$$

and

$$\mathbf{U}_{ib}(s,t) = \int_\Omega \mathbf{u}(\mathbf{x},t)\delta(\mathbf{x} - \mathbf{X}(s,t))d\Omega. \tag{8}$$

Eq. (7) is Goldstein's feedback law and according to (Goldstein et al., 1993), α and β are negative constants chosen to enforce the no-slip condition up to arbitrary small value and U_{ib} is the interpolated velocity at the Lagrangian points location. Eventually, in order to link the structural (Eqs. (3)–(5)) with the fluid part (Eqs. (1)–(2)), the forcing $\mathbf{f}(\mathbf{x},t)$ is evaluated from the Lagrangian forces by

$$\mathbf{f}(\mathbf{x},t) = \rho\int_\Gamma \mathbf{F}(s,t)\delta(\mathbf{x} - \mathbf{X}(s,t))ds. \tag{9}$$

Eqs. (8) and (9) link Lagrangian and Eulerian quantities through a convolution with a discretised version of Dirac delta function δ (see Peskin, 2002). Among a wide choice of synthetic delta functions, we make use of the one proposed by Roma et al. (1999). Note that the density difference in the dimensional version of Eqs. (1)–(3) (ρ_F^* and ρ_1^*, respectively) is taken into account in Eq. (9) through the ratio $\rho = \rho_1^*/(\rho_F^* L^*)$ (see Huang et al., 2007).

3.1. Boundary conditions

Boundary conditions for the fluid are given as follows; periodicity between $\partial\Omega_l$ and $\partial\Omega_r$ and $\{\mathbf{u} \cdot \mathbf{n} = 0, \partial(\mathbf{u} \cdot \tau)/\partial n = 0\}$ at $\partial\Omega_{top}$ and $\partial\Omega_{bottom}$ (imposed symmetry), where $\mathbf{n}$ and τ are respectively the normal and tangential directions to the boundary. Since the computational grid for the flow is staggered, no boundary conditions for the pressure are needed (see Natali et al., 2016). Hydrodynamical forces acting on the filaments are calculated by means of Goldstein's feedback law (see Goldstein et al., 1993), which enforces the no-slip condition up to an arbitrary small value. Since the filament is clamped to a moving plate with a given angle θ (see Fig. 3), Eq. (3) needs to be solved with proper boundary conditions, both at the clamped and at the free edge:

$$\mathbf{X}|_{s=0} = \mathbf{X}_p(t), \quad \frac{\partial \mathbf{X}}{\partial s}\bigg|_{s=0} = (\cos\theta, \sin\theta), \quad \frac{\partial^2 \mathbf{X}}{\partial s^2}\bigg|_{s=L} = 0, \quad \frac{\partial^3 \mathbf{X}}{\partial s^3}\bigg|_{s=L} = 0. \tag{10}$$

The first and second conditions enforce the filament to follow the underlying moving plate and to be clamped with a given angle θ, while the third and fourth conditions state that the bending moment and shear at the free edge is zero, respectively. The latter condition is true in both the tear and hole case. The two cases are, however, different in that for the tear case no further forces other than the hydrodynamical ones are applied at the free edge, while in the hole case the free edges are subject to an additional force $\pm k_\Sigma(\mathbf{X}_1 - \mathbf{X}_2)|_{s=L}$ (depending on the filament) modelling the tip-connecting spring. Eq. (5) is
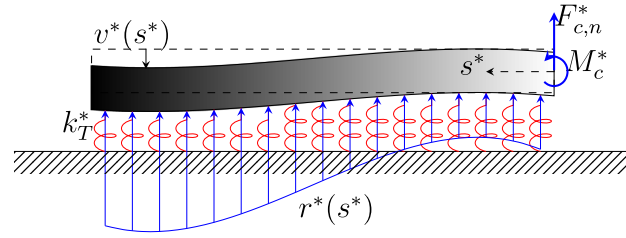
Fig. 4. Semi-infinite foundation (in grey) subject to a punctual force $F_{c,n}^*$ and moment M_c^* at the finite end (white), and supported by elastic spring of stiffness k_T^* (in red). The foundation reaction $r^*(s^*)$ (in blue) is proportional to the foundation displacement $v^*(s^*)$. (For interpretation of the references to colour in this figure legend, the reader is referred to the web version of this article.)

solved together with two conditions. The first, which is valid both for the GRT and the RH case, derives from Eq. (3) and is given as

$$\frac{\partial}{\partial s}\left(T\frac{\partial \mathbf{X}}{\partial s}\right)\bigg|_{s=0} = \mathbf{F} + \mathbf{F}_b + A_P, \tag{11}$$

where A_P is the plate acceleration. The second describes the tension at the filament end ($s = L$). In the GRT case the tension is zero, $T|_{s=0} = 0$, while in the hole case $T|_{s=0} = \Sigma(\mathbf{X}_1 - \mathbf{X}_2)$. The latter condition is an approximation of the real case since, numerically, the filament tip in the RH case is hinged to the tip-connecting spring. However, we have verified that the filament and the spring remain nearly tangent during the simulations so this should not introduce a significant error.

The main observables of this work are the forces and moments at the clamped edge of the filaments, defined as:

$$\mathbf{F}_c = (T\tau + S\mathbf{n})|_{s=0}, \quad M_c = k\gamma|_{s=0} \tag{12}$$

where S is the shear force, $\mathbf{n}$ and τ are the local normal and tangential unit vectors while k is the curvature of the filament at the clamped edge. In this way, the computed force $\mathbf{F}_c$ and moment M_c are those exerted by the filament on the plate.

3.2. Modelling the tendency to detach

The numerical model presented in Section 3 allows us to compute the dynamics of the fluid and filaments during the motion of the wall, including the fluid velocity, pressure, and the displacement of the filament in time. The main observables of the analysis are the clamping forces $\mathbf{F}_c$ and moment M_c exerted by the filament on the wall as these are the possible causes of further retinal detachment. In order to study the tendency of the filament(s) to further detach from the wall due to the combined actions of the wall-normal component of the clamping force, $F_{c,n}$, and torque, M_c, at the clamping point(s), we borrow from geotechnics the simple model of a structure on an elastic foundation (see Winkler, 1867). The model assumes that the substrate can be described as a system of identical, mutually independent, closely spaced, discrete and linearly elastic springs (see Fig. 4). In this way the substrate reaction $r^*(s^*)$ N/m^2 is proportional to the foundation displacement $v^*(s^*)$ through the spring stiffness constant k_T^*, $r^*(s^*) = -k_T^* v^*(^*s)$, since a negative displacement causes an upwards foundation reaction. In our specific case the foundation, representing the attached retina, will be considered as a semi-infinite beam, and the external loads $F_{c,n}^*$ and M_c^* from the filament are applied at its end. In this case the displacement $v^*(^*s)$ is found in closed form as

$$v^*(s^*) = \frac{e^{-\alpha^* s^*}}{2\alpha^{*3}B^*}(\alpha^* M_c^*[\cos(\alpha^* s^*) - \sin(\alpha^* s^*)] + F_{c,n}^*\cos(\alpha^* s^*)), \tag{13}$$

where B^* is the beam bending stiffness and α^* is the characteristic wave number defined as

$$\alpha^{*4} = \frac{k_T^* l^*}{4B^*}, \tag{14}$$

where l^* is the width of the model beam. Moreover, $B^* = E^* I^*$, where $I^* = h^{*3} l^*/12$ is the area moment of inertia of the filament cross section (here taken to be rectangular). In order to find a reasonable value of k_T^* we can write

$$r^*(s^*) = -E_T^*\epsilon = -E_T^*\frac{v^*(s^*)}{h_c^*},$$

where ϵ is the deformation of the compressible layer and h_c^* is its undeformed height. By definition we then get that $k_T^* = E_T^*/h_c^*$ and we can write

$$\alpha^{*4} = \frac{k_T^* l^*}{4B^*} = \frac{E^* l^*}{4h_c^* E^* I^*} = \frac{l^*}{4h_c^* h^{*3} l^*/12} = \frac{3}{h_c^* h^{*3}},$$

Table 2
Values of dimensionless parameters used in the simulations.

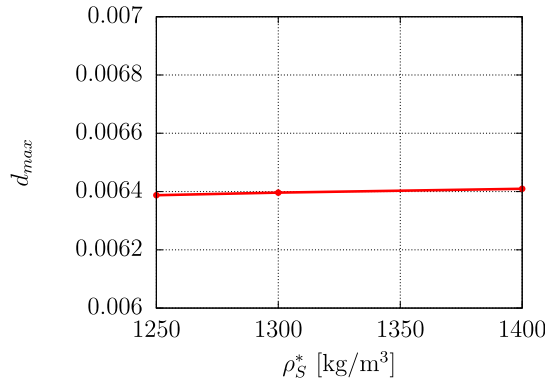| L^* [mm]	γ	Re	ρ
8 degrees saccade			
1.50	0.197	85.92	0.014
1.75	0.145	100.23	0.012
2.00	0.111	114.55	0.011
2.25	0.088	128.87	0.009
2.50	0.071	143.19	0.008
15 degrees saccade			
1.50	0.108	116.06	0.014
1.75	0.079	135.40	0.012
2.00	0.061	154.74	0.011
2.25	0.048	174.08	0.009
2.50	0.039	193.43	0.008

Fig. 5. Maximum tendency to detach d_{max} over time in the case of GRT during a 8 degrees saccade, for different values of the retina density ρ_s^* and $\theta = 33.56°$. The value used from here on is $\rho_s^* = 1300$ [kg/m³].

where we have simply substituted E_T^* with E^*. If we further assume that $h_c^* = h^*$ then $\alpha^{*4} = 3/h^{*4}$. In the simulations presented here $h = h^*/L^* = 1/30$ which gives $\alpha = \alpha^*L^* \simeq 40$. However, the conclusions drawn in this paper are quite insensitive to the value of α. We now define, on dimensional form, as *tendency to detach* the upward displacement d^* of the finite end ($s^* = 0$), thus

$$d^*(t^*) = \max(\left. v^*\right|_{s^*=0}, 0) = \max\left(\frac{\alpha^*M_c^*(t^*) + F_{c,n}^*(t^*)}{2\alpha^{*3}B^*}, 0\right). \tag{15}$$

Note that d^* is a function of time and must be evaluated during the whole plate motion in order to find the overall maximum value and the corresponding instant at which it occurs, here denoted d_{max}^* and t_{max}^*, respectively. The force $F_{c,n}^*(t^*)$ is evaluated from the tension $T^*(s^*, t^*)$ and shear force $S^*(s^*, t^*)$ at the clamping point according to

$$F_{c,n}^*(t^*) = T_c^*(t^*)\sin\theta + S_c^*(t^*)\cos\theta. \tag{16}$$

3.3. Solution procedure

At each time step the numerical algorithm can be summarised as follows:

1. evaluation of hydrodynamical forces **F** on the filament (Eqs. (6)–(8)) to enforce the no-slip condition up to a given value (see Section 3.4);
2. spreading of the force **F** from Lagrangian points on the Eulerian grid (Eq. (9));
3. solution of fluid flow (Eqs. (1) and (2));
4. solution of filament motion (Eqs. (3) and (5)).

3.4. Numerical discretisation

The computational domain is $5L \times 2.5L$ (horizontal $\times$ wall-normal direction) in the GRT case, while it is $6L \times 2.5L$ in the case of RHs. In our simulations the 2D mesh for the fluid is uniform along the plate with grid spacing $1/60$, while in the
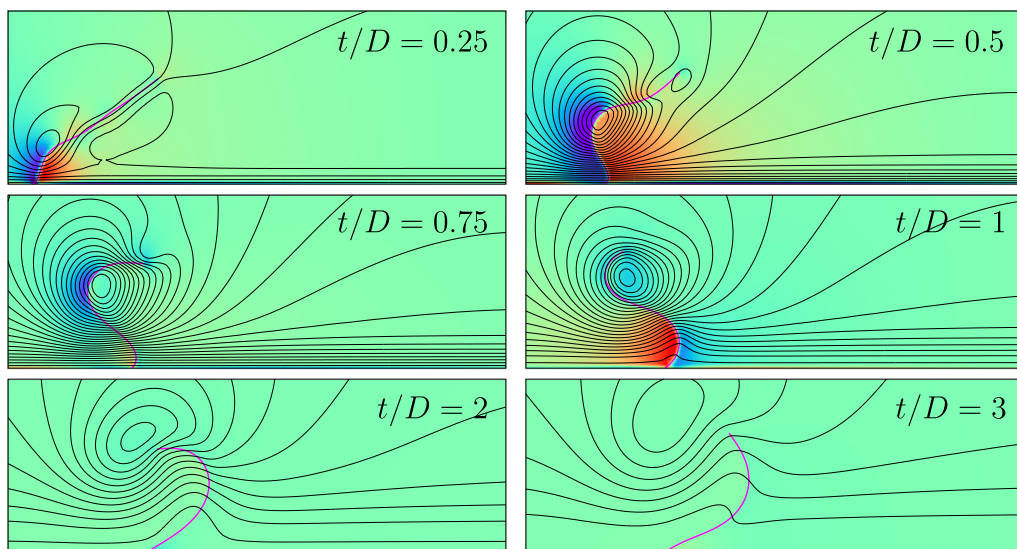
Fig. 6. Configurations attained at different times by the retinal flap with $L^* = 2$ mm, $\theta = 33.56°$. The wall moves from left to right. The duration of the simulation is $5D$, with D duration of the saccadic movement. The times at which the flap configuration are shown are: $t^*/D^* = 0.25, 0.6, 0.75, 1, 2, 3$. Solid black lines represent streamlines, locally tangential to the flow field, while colours represent the pressure field (red $= 0.5$, blue $= -0.5$). (For interpretation of the references to colour in this figure legend, the reader is referred to the web version of this article.)

normal direction it is uniform in the region [0, 1.5] with grid spacing 1/40 and stretched outside with a constant stretching ratio equal to 1.1. On the other hand, the 1D filament mesh is made of 120 points uniformly distributed along the curvilinear coordinate of the filament. In order to reach a trade-off between CFL number for numerical stability ($\sim 10^{-2}$) and non-slip enforcement ($\sim 10^{-2}$), the Goldstein's feedback law coefficients has been set to $\beta_1 = -10$ and $\beta_2 = -10^2$. To solve the incompressible Navier–Stokes equations we make use of the fractional step method (Natali et al., 2016; Chorin, 1968; Perot, 1993; Temam, 1968).

4. Numerical results

We solved the mathematical model numerically, using the parameters presented in Table 1 for two different saccadic motions, 8 and 15 degrees. The corresponding dimensionless parameters γ, Re and ρ are presented in Table 2. Moreover, in all calculations the effect of gravity was neglected and the plate motion was from left to right. The considered wall motion is the worst-case scenario in terms of the reacting force in the wall-normal direction, as well as the moment. An opposite motion is likely to create larger shear forces at the attachment point that, for the current definition of detachment, is of less interest. Simulations were performed by varying the clamping angle θ, the length of the detached retina L^*, and the inter-tip distance Δ^* (in the case of RHs) in order to understand which cases are more prone to further detachment. A convergence study of the spatial and temporal resolutions has been performed for all results shown here (see Natali et al., 2016). In Fig. 5 we show that the tendency to detach $d_{max} = d^*_{max}/L^*$, which is the main observable of the analysis, is quite insensitive to changes of density for the filament studied here.

4.1. The case of GRT

Results from the simulations regarding the giant retinal tear are presented in this section and snapshots showing the dynamics of the free flap are shown in Fig. 6, which also indicates the streamlines of the flow and the fluid pressure. In this case the flap has the length $L^* = 2$ mm. At the initial time, just before the wall is set into motion, the GRT flap is a straight line forming an angle θ with the wall, and we assume $\theta = 33.56°$. During the accelerating phase of the wall (motion of the wall is from left to right) the flap is deflected to the left by fluid flow. Initially the deflection is larger in the region close to the wall and progressively interests all the length of the flap as the motion continues. The wall motion stops at $t^*/D^* = 1$ and the flap motion thereafter continues for a while due to inertial effects. The evolution of the force and moment that are generated at the clamping point as a function of time are presented in Fig. 7 in comparison with $d = d^*/L^*$. The terms regarding the force and moment are normalised by $2\alpha^{*3}B^*L^*$, according to Eq. (15), in order to facilitate a direct comparison. The clamping moment grows until approximately the instant of maximum velocity ($t^*/D^* \approx 0.5$). Owing to inertia, the fluid that is set in motion by the saccade continues to move after the plate has come to rest. This results in a change of sign of the force and moment at some instant, which could be either before or after the plate comes to a halt. The signs of the terms $F^*_{c,n}/2\alpha^{*3}B^*L^*$ and $\alpha^*M^*_c/2\alpha^{*3}B^*L^*$ are not necessarily the same at each instant in time and this is reflected in the value taken
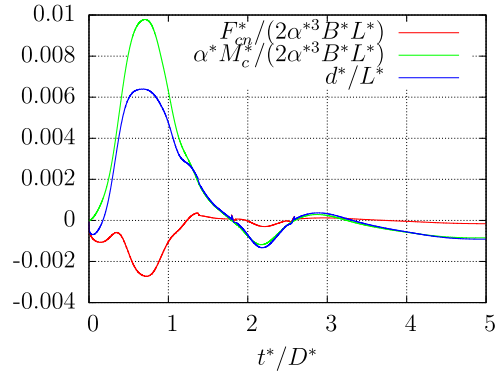
Fig. 7. The three terms; tendency to detach, force and moment, from Eq. (15), normalised for direct comparison and made dimensionless using the reference length L^*, all as a function of the dimensionless time t^*/D^*. In this case $L^* = 2$ mm and $\theta = 33.56°$.
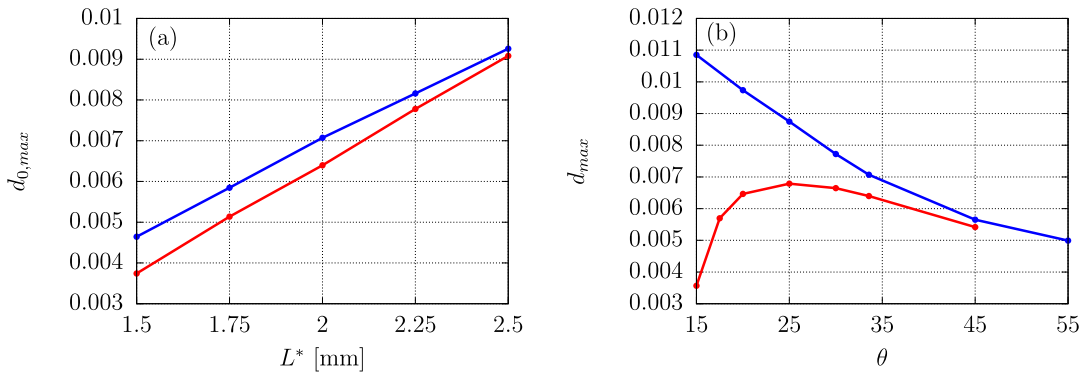

Fig. 8. Maximum tendency to detach over time, for the GRT case (a) $d_{0,max}$ comparing different values of the flap length L^*, with $\theta = 33.56°$ in all cases, (b) d_{max} for different values of the clamping angle θ, and $L^* = 2$ mm in all cases. In both figures red and blue refer to the 8 and 15 degrees saccades, respectively. (For interpretation of the references to colour in this figure legend, the reader is referred to the web version of this article.)

by the tendency to detach d. In this particular case, the term proportional to M_c^* is dominant in the expression for d, and this can be appreciated in Fig. 7, where the time evolution of $\alpha^* M_c^* / 2\alpha^{*3} B^* L^*$ and d are similar, especially during the saccadic motion. The instant of maximum d approximately coincides with that of $\alpha^* M_c^* / 2\alpha^{*3} B^* L^*$ ($t^*/D^* \approx 0.5$).

4.1.1. The effect of changing the flap length

The length L^* of the detached retina can vary and here we investigate the effect of the length on the tendency to detach. Note that in this case the results are shown in terms of $d_0 = d^*/L_0^*$, where $L_0^* = 2$ mm. In Fig. 8a, we show the maximum value: $d_{0,max} = d_{max}^*/L_0^*$ over time, for different flap lengths, using a fixed angle $\theta = 33.56°$. The results show that $d_{0,max}$ increases with increasing L^*, indicating that longer detached retinal flaps are more prone to detach further than shorter ones. In the same figure, results are shown for two different saccadic amplitudes, 8 and 15 degrees, respectively. As the amplitude of the saccadic motion increases, so does the value of $d_{0,max}$.

4.1.2. The effect of changing the clamping angle

The clamping angle θ can also vary in reality and a graph of d_{max} over time, as a function of θ is shown in Fig. 8b. The results show that, for a saccadic motion of 8 degrees, flaps at an angle of around $\theta \approx 25°$ have the highest tendency to detach, with the tendency decreasing away from this value. For a saccadic motion of 15 degrees, instead, the behaviour is quite different. The value of d_{max} increases as the angle is decreased, at least for the values of angles analysed here. In both saccadic motions the moment prevails on the normal force when evaluating d_{max}. However, in the case of 15 degrees amplitude, the moment remains fairly constant (not shown here) while the normal force gets increasingly negative. In the case of 8 degrees, instead, the moment increases with increasing clamping angle. The moment is proportional to the curvature. This means that when the saccadic amplitude is large, which results in a larger plate velocity, the curvature at the clamping point is almost independent of the clamping angle, and the plate velocity prevails on the initial configuration of the filament.
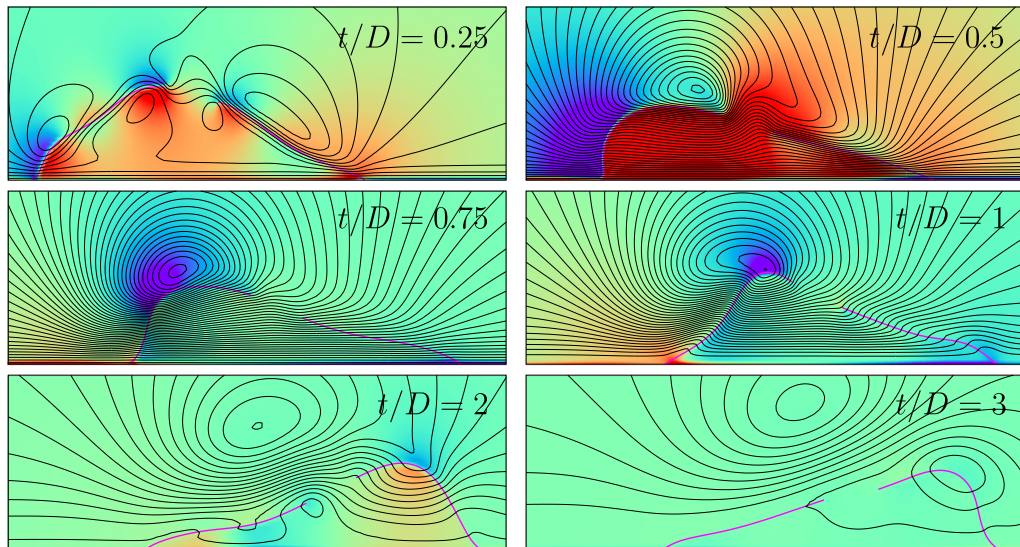
Fig. 9. Dynamics of the RH case during eye movement. For parameter values see Fig. 6. (For interpretation of the references to colour in this figure legend, the reader is referred to the web version of this article.)

4.2. The case of RH

When the wall is set into motion the retinal flaps deform under both fluid and elastic forces also in the case of a retinal hole, but the resulting shape is quite different compared to the GRT case. This can be seen in Fig. 9 where snapshots of the dynamics are presented, for a given case, in terms of streamlines of the flow and pressure distribution. In the case presented, the flap length is $L^* = 2$ mm, the clamping angle $\theta = 33.56°$ and the inter-tip distance $\Delta^* = 0.17$ mm. In the acceleration phase ($t^*/D^* < 0.5$) the left flap is pushed back by the fluid and the pressure in the detachment region builds up. In the decelerating phase ($0.5 < t^*/D^* < 1$) the fluid continues to move towards the right due to inertial effects, inflating the right filament and producing a smaller pressure rise. In what follows we present results of the tendency to detach d by varying L^*, θ and Δ^*. For all cases investigated here we found that the maximum value of d of the left flap was always larger than that of the right flap, independently of the saccadic amplitude. In the following we, therefore, only show results from the left flap.

4.2.1. The effect of changing the length of the detached retina

The effect of changing the length L^* of the detached retina is here investigated for the case of RH. We use, as in the case of GRT, as baseline value $L_0^* = 2$ mm. The clamping angle, on both sides, is held constant with a value of $\theta = 33.56°$ and the inter-tip distance is set to $\Delta^* = 0.17$ mm. The instant at which the peak value of $d_0 = d^*/L_0^*$ is found changes with the value of L^*; the longer is L^* the later the peak value of d occurs. The maximum values of d_0, for each case are reported in Fig. 10a as function of L^* and saccadic amplitude. A clear increase in the maximum value of d is found as the value of L^* is increased indicating that longer detached retinal flaps, meaning that wider and deeper hole cavities are more prone to detach compared to smaller ones. This is enhanced as the saccadic amplitude is increased.

4.2.2. The effect of changing the inter-tip distances

Changing the inter-tip distance Δ^*, while keeping $L^* = 2$ mm and $\theta = 33.56°$ constant in the numerical model, corresponds to different diameters of a RH. Fig. 10b shows that the maximum value of d over time, does not depend significantly on Δ^*, suggesting that the overall size of a hole is of relatively little importance regarding its tendency to detach. One could argue that this might not be the case for shorter filaments, i.e. for increasing values of Δ^*/L^*. To test this we also made simulations using $L^* = 1.5$ mm, and $\theta = 33.56°$. The results are reported in Fig. 10b and it is shown that, even in this case, the value of Δ^* has a week influence on d.

4.2.3. The effect of changing the clamping angles

The effect of changing the clamping angles is shown in Fig. 10c, with $L^* = 2$ mm and $\Delta^* = 0.17$ mm fixed. In all cases the values of θ are the same for the left and right flaps. In this case a maximum value of d is found, for both saccadic amplitudes, and the corresponding clamping angle is $\theta \approx 35°$.
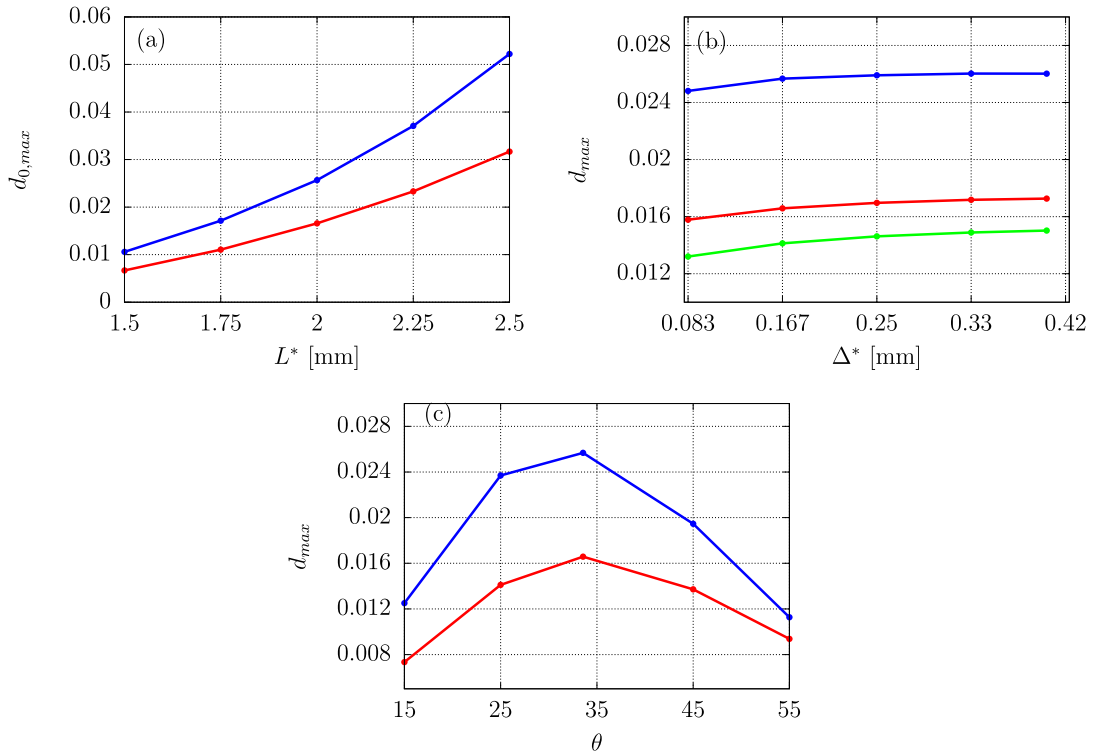
Fig. 10. Maximum values of the tendency to detach for the hole case (left flap) for (a) $d_{0,max}$ for different lengths L^* while keeping $\Delta^* = 0.17$ mm and $\theta = 33.56°$ constant (red curve: 8 deg. saccade, blue curve: 15 deg. saccade), (b) d_{max} for different inter-tip distance Δ^* with $\theta = 33.56°$ and $L^* = 2$ mm (red curve: 8 deg. saccade, blue curve: 15 deg. saccade), $L^* = 1.5$ mm (green curve: 15 deg. saccade), (c) d_{max} for different clamping angles θ with $L^* = 2$ mm and $\Delta^* = 0.17$ mm constant (red curve: 8 deg. saccade, blue curve: 15 deg. saccade). (For interpretation of the references to colour in this figure legend, the reader is referred to the web version of this article.)
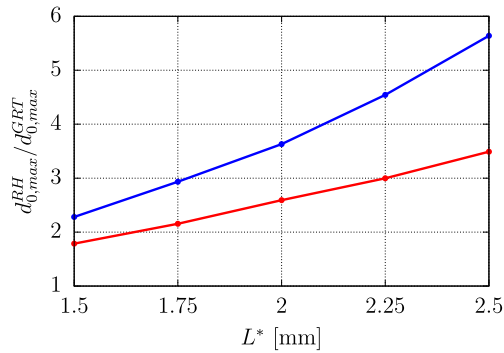

Fig. 11. Ratio of the maximum tendency to detach between the RH and GRT cases for different flap lengths L^* keeping $\theta = 33.56°$ and $\Delta^* = 0.17$ mm constant. Here, red and blue curves refer to the 8 and 15 degrees saccade, respectively. (For interpretation of the references to colour in this figure legend, the reader is referred to the web version of this article.)

4.3. Comparison between the GRT and RH

It has been clinically observed that the tendency to further detach is larger in the case of a RH than a GRT. The fovea off rate for rhegmatogenous retinal detachment excluding GRT is 56% (Williamson et al., 2014) whereas the fovea off rate for GRT has been reported as 45.2% (Ang et al., 2010). Therefore, it is possible that, despite the much larger size of the GRT, its tendency to extend to the central retina is less than for other types of breaks. This is investigated here by keeping all parameters equal in both cases. The only additional parameter used in the hole case is the inter-tip distance, which was fixed at $\Delta^* = 0.17$ mm. This should, however, not influence the results since it has already been shown in Section 4.2.2 that the value of Δ^* does not affect much the results. The comparison of the maximum tendency to detach between the RH and the GRT cases are presented in Fig. 11 for different values of L^*, and two different saccadic amplitudes. In the investigated

range of flap lengths, the RH configuration has a tendency to detach between 2 and 3.5 times that of the GRT case, for 8 degrees saccades, and 2–5.5 times that of GRT for 15 degrees saccades (for increasing values of the detached retinal length L^*), which somewhat explains clinical observations.

5. Conclusions

Recognising the patterns of the development of a condition is essential for its efficient management. This is especially true for retinal detachment for which disorder little is understood about progression mechanisms. Testing features of the retinal detachment as we have done in the numerical investigations presented in this paper can help prioritise surgery and chose surgical methodology. The surgeon on examination of the retina can make judgements on the contours and extent of the detachment, and the angle of attachment of the retina to the underlying structures. Some detachments have shallow retinal elevation of the retina and others have bullous elevations, some are small in area and others large, retinas may be stiff or mobile and RHs small or large. The surgeon cannot effectively interpret the findings of the examination of the eye without modelling these parameters for their effect on the behaviour of the retina.

In this paper we considered two particular cases: a free flap giant retinal tear (GRT) consisting of a single detached flap with a large circumferential extent, and a retinal hole (RH). In our idealised model we consider a cross section of the real detachment resulting in a two-dimensional model. In this context the retinal flap is described as a one-dimensional massive object, with a given bending stiffness, attached at a certain angle at one end on the retinal wall. The flap is 30% heavier than the surrounding fluid, the length is 1.5–2.5 mm and the thickness 70 μm. Other relevant parameters are taken from the literature in order to model as close as possible realistic situations. The curvature of the vitreous chamber is neglected, so the retinal wall is assumed to be flat and rigid. Moreover, we assume the case of a liquefied vitreous with a domain extending to infinity in the wall-normal direction. The liquified vitreous is assumed to be a purely viscous fluid, with the same properties as water, and the fluid flow is generated by a saccadic eye rotation of the retinal wall (see Repetto et al., 2005). Three-dimensional effects in the case of a retinal free flap are expected to be weak, but in the case of a RH we model the three dimensionality in a highly simplified way, by limiting the maximum distance between the two free flap tips. This simplified model is supposed to mimic the effect of the hole: the tips can get closer to each other (closing the hole) but not separate (opening the hole) too much. In all simulations we monitor the forces and moment exerted by the flap on the retinal wall at the clamping point(s). In particular, the normal component of the force together with the moment are used to evaluate the *tendency to detach* using Winkler's theory, i.e. considering the pigment epithelium as an elastic foundation on which the retina is attached. This model gives an expression for displacement of the elastic foundation as a function of the distance from the clamping point and we define the tendency to detach as the displacement at the clamping point.

We analysed the tendency to detach for both the free flap and the hole case for different values of the detached retinal length, clamping angle and inter-tip distance (in the case of a RH), and two different saccadic amplitudes. The general conclusions can be summarised as follows:

- The tendency to detach increases as the retinal flap length increases, both for the RH and the GRT.
- The worst-case angle that gives rise to the greatest tendency to detach is found to be around 25° for GRT, when a 8 degrees saccade is imposed, and around 35° for a RH, independently of the saccadic amplitude.
- The effect of changing the inter-tip distance (related to the size of the retinal hole) on the tendency to detach is weak, also when decreasing the filament length L^*.
- The tendency to detach of a RH, compared to a GRT, is 2–3.5 times larger for retinal flaps of 1.5–2.5 mm, and the ratio increases for longer flap lengths. This ratio increases as the saccadic amplitude is increased.

This work is based on a highly simplified description of the real case and further work is certainly needed to make the model more realistic. For instance, the simplified displacement-type evaluation used to determine the tendency to detach could be improved considering a model that accounts for detachment progression. In this case a force/stress-type criterion would be more appropriate. However, in spite of its simplicity, the model accounts for ingredients that were disregarded in previous attempts to model the mechanics of RRD and that we believe are essential to capture some of the physics involved. In particular for the first time, the dynamics of a detached retina is studied as a fluid–structure interaction problem. We believe that this model advances our understanding on the mechanics of RRD an represents a useful step towards more refined and geometrically accurate models.

Acknowledgements

References

Abouali, O., Modareszadeh, A., Ghaffariyeh, A., Tu, J., 2012. Numerical simulation of the fluid dynamics in vitreous cavity due to saccadic eye movement. Med. Eng. Phys. 34 (6), 681–692.
Alamouti, B., Funk, J., 2003. Retinal thickness decreases with age: an OCT study. Br. J Ophthalmol. 87 (7), 899–901.
Ang, G., Townend, J., Lois, N., 2010. Epidemiology of giant retinal tears in the United Kingdom: the British Giant Retinal Tear Epidemiology Eye Study (BGEES). Invest. Ophthalmol Vis. Sci. 51 (9), 4781–4787.

Angunawela, R.I., Azarbadegan, A., Aylward, G.W., Eames, I., 2011. Intraocular fluid dynamics and retinal shear stress after vitrectomy and gas tamponade. Invest. Ophthalmol Vis. Sci. 52 (10), 7046–7051.

Bottega, W.J., Bishay, P.L., Prenner, J.L., Fine, H.F., 2013. On the mechanics of a detaching retina. Math. Med. Biol. 30 (4), 287–310.

Bowd, C., Weinreb, R.N., Lee, B., Emdadi, A., Zangwill, L.M., 2000. Optic disk topography after medical treatment to reduce intraocular pressure. Am. J. Ophthalmol. 130 (3), 280–286.

Chorin, A.J., 1968. Numerical Solution of the Navier-Stokes Equations. Math. Comp. 22, 745–762.

Dogramaci, M., Williamson, T.H., 2013. Dynamics of epiretinal membrane removal off the retinal surface: a computer simulation project. Br. J. Ophthalmol. 97 (9), 1202–1207.

Eames, I., Angunawela, R.I., Aylward, G.W., Azarbadegan, A., 2010. A theoretical model for predicting interfacial relationships of retinal tamponades. Invest. Ophthalmol. Vis. Sci. 51 (4), 2243–2247.

Ethier, C.R., Johnson, M., Ruberti, J., 2004. Ocular biomechanics and biotransport. Annu. Rev. Biomed. Eng. 6, 249–273.

Fauci, L.J., Peskin, C.S., 1988. A computational model of aquatic animal locomotion. J. Comput. Phys. 77, 85–105.

Foster, W.J., 2011. Bilateral patching in retinal detachment: fluid mechanics and retinal "settling". Invest. Ophthalmol. Vis. Sci. 52 (8), 5437–5440.

Foster, W.J., Dowla, N., Joshi, S.Y., Nikolaou, M., 2010. The fluid mechanics of scleral buckling surgery for the repair of retinal detachment. Graefe's Arch. Clin. Exp. Ophthalmol. 248 (1), 31–36.

Goldstein, D., Handler, R., Sirovich, L., 1993. Modeling a no-slip flow boundary with an external force field. J. Comput. Phys. 105, 354–366.

Huang, W.-X., Shin, S.J., Sung, H.J., 2007. Simulation of flexible filaments in a uniform flow by the immersed boundary method. J. Comput. Phys. 226, 2206–2228.

Isakova, K., Pralits, J.O., Repetto, R., Romano, M.R., 2014. Mechanical models of the dynamics of vitreous substitutes. Bio. Med. Res. Int. 2014.

Jones, I.L., Warner, M., Stevens, J.D., 1992. Mathematical modelling of the elastic properties of retina: a determination of Young's modulus. Eye 6, 556–559.

Kim, Y., Peskin, C.S., 2007. Penalty immersed boundary method for an elastic boundary with mass. Phys. Fluids 19, 053103.

Kovacs, S.J., McQueen, D.M., Peskin, C.S., 2001. Modeling cardiac fluid dynamics and diastolic function. Philos. Trans. R. Soc. Lond. Ser. A Math. Phys. Eng. Sci. 359, 1299–1314.

Meskauskas, J., Repetto, R., Siggers, J.H., 2012. Shape change of the vitreous chamber influences retinal detachment and reattachment processes: Is mechanical stress during eye rotations a factor? Invest. Ophthalmol. Vis. Sci. 53 (10), 6271–6281.

Mitry, D., Chalmers, J., Anderson, K., Williams, L., Fleck, B.W., Wright, A., Campbell, H., 2009. Temporal trends in retinal detachment incidence in scotland between 1987 and 2006. Br. J. Ophthalmol. 95 (3), 365–369.

Modarreszadeh, A., Abouali, O., 2014. Numerical simulation for unsteady motions of the human vitreous humor as a viscoelastic substance in linear and non-linear regimes. J. Non-Newton. Fluid Mech. 204, 22–31.

Natali, D., Pralits, J.O., Mazzino, A., Bagheri, S., 2016. Stabilizing effect of porosity on a flapping filament. J. Fluids Struct. 61, 362–375.

Perot, J.B., 1993. An analysis of the fractional step method. J. Comput. Phys. 108, 51–58.

Peskin, C.S., 2002. The immersed boundary method. Acta Numer. 1–39.

Reichenbach, A., Eberhardt, W., Scheibe, R., Deich, C., Seifert, B., Reichelt, W., Dähnert, K., Rödenbeck, M., 1991. Development of the rabbit retina. IV. Tissue tensility and elasticity in dependence on topographic specializations. Exp. Eye Res. 53 (2), 241–251.

Repetto, R., Siggers, J.H., Stocchino, A., 2010a. Mathematical model of flow in the vitreous humor induced by saccadic eye rotations: effect of geometry. Biomech. Model. Mechanobiol. 9 (1), 65–76.

Repetto, R., Stocchino, A., Cafferata, C., 2005. Experimental investigation of vitreous humour motion within a human eye model. Phys. Med. Biol. 50, 4729–4743.

Repetto, R., Tatone, A., Testa, A., Colangeli, E., 2010b. Traction on the retina induced by saccadic eye movements in the presence of posterior vitreous detachment. Biomech. Model. Mechanobiol. 10, 191–202.

Roma, A.M., Peskin, C.S., Berger, M.J., 1999. An adaptive version of the immersed boundary method. J. Comput. Phys. 153, 509–534.

Shunmugam, M., Shunmugam, S., Williamson, T.H., Laidlaw, D.A., 2011. Air-gas exchange reevaluated: clinically important results of a computer simulation. Invest. Ophthalmol. Vis. Sci. 52 (11), 8262–8265.

Sigal, I.A., Flanagan, J.G., Ethier, C.R., 2005. Factors influencing optic nerve head biomechanics. Invest. Ophthalmol. Vis. Sci. 46 (11), 4189.

Temam, R., 1968. Une méthode d'approximation des solutions des équations Navier-Stokes. Bull. Soc. Math. France 98, 115–152.

Williamson, T.H., Lee, E.J., Shunmugam, M., 2014. Characteristics of rhegmatogenous retinal detachment and their relationship to success rates of surgery. Retina 34 (7), 1421–1427.

Williamson, T.H., Shunmugam, M., Rodrigues, I., Dogramaci, M., Lee, E., 2013. Characteristics of rhegmatogenous retinal detachment and their relationship to visual outcome. Eye 27 (9), 1063–1069.

Winkler, E., 1867. Die Lehre Von Elasticitaet Und Festigkeit. H. Dominicus, Prague.

Wollensak, G., Eberhard, S., 2004. Biomechanical characteristics of retina. Retina 24 (6), 967–970.

Zhu, L., Peskin, C.S., 2002. Simulation of a flapping flexible filament in a flowing soap film by the immersed boundary method. J. Comput. Phys. 179, 452–468.